

Article

Multi-Sensor Satellite Analysis for Landslide Characterization: A Case of Study from Baipaza, Tajikistan

Francesco Poggi^{1,*} , Olga Nardini¹, Simone Fiaschi² , Roberto Montalti³, Emanuele Intrieri¹ 
and Federico Raspini¹

¹ Department of Earth Sciences, University of Florence, DST UNIFI, Via Giorgio La Pira 4, 50121 Florence, Italy; olga.nardini@unifi.it (O.N.); emanuele.intrieri@unifi.it (E.I.); federico.raspini@unifi.it (F.R.)

² TRE ALTAMIRA, 475 W Georgia St #410, Vancouver, BC V6B 4M9, Canada; simone.fiaschi@tre-altamira.com

³ TRE ALTAMIRA, C/de Còrsega, 381, 08037 Barcelona, Spain; roberto.montalti@tre-altamira.com

* Correspondence: francesco.poggi1@unifi.it; Tel.: +39-3208834396

Abstract: Central Asia, and in particular Tajikistan, is one of the most geologically hazardous areas in the world, particularly in terms of seismicity, floods, and landslides. The majority of landslides that occur in the region are seismically induced. A notable site is the Baipaza landslide, which has been subject to deformation since the 1960s, with the most recent collapse occurring in 2002. The potential collapse of the landslide represents a significant risk to the nearby Baipaza hydroelectric dam, situated 5 km away, and has the potential to create widespread challenges for the entire region. The objective of this work is to provide a comprehensive characterization of the Baipaza landslide through the utilization of satellite remote-sensing techniques, exploiting both Sentinel-1 Synthetic Aperture Radar (SAR) and Sentinel-2 optical images freely available from the European Space Agency's (ESA) Copernicus project. The employment of these two techniques enables the acquisition of insights into the distinctive characteristics and dynamics of the landslide, including the displacement rates up to 246 mm/year in the horizontal component; the precise mapping of landslide boundaries and the identification of distinct sectors with varying deformation patterns; and an estimation of the volume involved within the landslide, which is approximately of 1 billion m³.



Academic Editor: Zhong Lu

Received: 14 April 2025

Revised: 4 June 2025

Accepted: 5 June 2025

Published: 10 June 2025

Citation: Poggi, F.; Nardini, O.; Fiaschi, S.; Montalti, R.; Intrieri, E.; Raspini, F. Multi-Sensor Satellite Analysis for Landslide Characterization: A Case of Study from Baipaza, Tajikistan. *Remote Sens.* **2025**, *17*, 2003. <https://doi.org/10.3390/rs17122003>

Copyright: © 2025 by the authors. Licensee MDPI, Basel, Switzerland. This article is an open access article distributed under the terms and conditions of the Creative Commons Attribution (CC BY) license (<https://creativecommons.org/licenses/by/4.0/>).

Keywords: landslide; SAR interferometry; Sentinel-1; COSI-Corr; Sentinel-2

1. Introduction

Central Asia ranks among the world's most geologically hazardous regions, facing significant threats from seismic activity, flooding, and landslides [1,2]. The region's location within the Eurasian–Indian continental collision zone is a key geological factor contributing to the elevated hazard. The northward collision of the Indian Plate with the Eurasian Plate generates a wide range of geological hazards [3,4]. This collision has led to the formation of a highly mountainous terrain, a defining feature of the region, characterized by ongoing deformation; active faulting; and frequent, strong earthquakes [5]. Consequently, the complex geological structures, rugged landscape, and high seismicity of these areas make large landslides a likely occurrence [6].

Studies on landslides [7,8], avalanches [9], and earthquakes [10] have shown that one of the most affected areas of Central Asia is Tajikistan. This is due to a combination of its geographical and geomorphological features, including high mountains that are characterized by continuous deformation and deep intermountain depressions that separate mountain ridges [11]. The majority of landslides affecting Tajikistan are rotational/translational

slides, rock avalanches, and mud/debris flows [12]. These are caused by intense rainfall, earthquakes, or snowmelt [13]. They are identified as the third most dangerous natural hazard in the country, after earthquakes and floods [2]. Furthermore, an analysis of the landslides that have occurred in the area has identified certain sites that are particularly susceptible to this type of hazard, with recurrent events occurring in locations such as Baipaza, Maylusuu, and Naugarzan [14]. Landslides are the result of a complex interplay of several factors, including geology, topography, seismic activity, and geomorphology [15], and can have significant socio-economic and environmental consequences at the national level [16].

This study investigates the Baipaza landslide in the Tajik Depression, a site of significant concern due to the landslide's size and potential to create a river dam upon failure. The proximity of the Baipaza dam, a crucial infrastructure of Tajikistan, further heightens this concern, as its stability could be compromised. Considering the area's challenging topography, remote-sensing techniques emerge as effective and valuable methods for analyzing and studying this inaccessible region.

In order to provide a comprehensive overview of the Baipaza landslide, two remote-sensing techniques were employed. The first is the Interferometric Synthetic Aperture Radar (InSAR), a powerful tool for detecting and measuring Earth surface changes with millimetric precision [17], including subsidence [18,19], landslides [20], earthquakes [21], and glacier movement [22]. In particular, we used the SqueeSAR [23] algorithm, an evolved form of traditional multitemporal InSAR techniques. It leverages radar backscattering information from both the Permanent Scatterers (PSs), which include strong reflectors like buildings and rock outcrops, and the Distributed Scatterers (DSs), which encompass areas exhibiting low but consistent backscattering, such as low vegetation or bare soil. A fundamental aspect of the SqueeSAR is the distinction between PS and DS, which relies on different statistical methods. A key advantage of InSAR is its capability to generate displacement time series over extended periods by combining data from multiple SAR acquisitions [24]. The application of statistical methodologies, including the Principal Component Analysis (PCA) and the K-means algorithm, on the InSAR time series allows for the identification of various displacement patterns. The PCA is a statistical technique that involves the reduction of data dimensionality through the identification of combinations of features that effectively characterize multivariate samples [25] by balancing between the loss of information and the optimal number of dimensions to preserve [26]. The methodology was initially introduced by [27], especially for physical, statistical, and biological investigation, and it has since been applied also to landslides and geological analysis.

The second technique under consideration is the Co-Registration of Optically Sensed Images and Correlation (COSI-Corr) method [28]. This module has been integrated into ENVI 6.0, which is regarded as one of the most effective software tools for imagery processing due to its wide range of functionality for preprocessing, processing, and postprocessing of images. The range of services offered by ENVI includes land-use mapping, change detection, spectral index computation, satellite-image classification, and the creation of geographic and environmental maps. The COSI-Corr is a tool designed to identify ground deformation in multitemporal acquisitions and to achieve precise geometrical processing of optical satellite and aerial images through orthorectification, co-registration, and correlation processes. COSI-Corr finds applications in landslides [29], glacier flows [30], and change detections that demand accurate image registration [31].

In this study, we investigate the ground deformation at the Baipaza landslide, using imagery from the ESA's Sentinel-1 and Sentinel-2 satellite constellations. Sentinel-1 consists of two identical satellites, Sentinel-1A (launched April 2014) and Sentinel-1B (launched April 2016; decommissioned December 2021 due to a power issue), both carrying C-band

SAR sensors [32,33]. They orbit in similar planes, with a 12-day revisit time, which is reduced to 6 days when both satellites are operational. Sentinel-1 provides a ground resolution of roughly 5×15 m in the range and azimuth directions, respectively [33]. For our InSAR analysis, we acquired and processed 147 ascending and 142 descending SAR images from October 2014 to October 2020, covering an area of approximately 50 km². Sentinel-2 consists of a high-resolution multispectral imaging mission designed for land monitoring, consisting of a pair of twin satellites. It provides detailed imagery for observing vegetation, soil, water bodies, inland waterways, and coastal regions [34]. Sentinel-2A was launched on 23 June 2015, followed by Sentinel-2B on 7 March 2017. The satellites carry sensors capable of capturing data across 13 spectral bands, spanning from the visible to the shortwave infrared (SWIR) range. The mission offers revisit times between 5 and 10 days. Two Sentinel-2 images were collected on the dates of 26 July 2016 and 29 August 2022, covering the entire period of the InSAR data to guarantee a complete comparison of the results. This period was selected to satisfy several requirements: firstly, acquisition during the summer season, as the study area is located at high altitudes, and consequently, in winter, the presence of snow cover could make the analysis impossible; secondly, the presence of cloud cover in the summer season further reduced the available image dataset; and finally, the intention was to select a pair of scenes with the widest possible temporal baseline.

The integration of SAR and optical data, covering a wide range of displacement regimes, provides valuable supplementary insights. This approach bridges the gaps of each individual technique and contributes to a more in-depth investigation of the area's displacement. Although the Baipaza landslide is a known phenomenon, comprehensive mapping, velocity estimation, and characterization of its movements have been lacking. Therefore, this study represents an initial effort toward such an analysis.

2. Study Area

The Baipaza landslide is situated within the Tajik depression, in the western region of Tajikistan (Figure 1). From a geological perspective, the Tajik depression is characterized by a diverse range of rock formations, including Jurassic evaporites; Lower Cretaceous cross-bedded red sandstone; Upper Cretaceous and Paleogene interbedded limestone, shale, and gypsum; and Neoproterozoic quartzose molasse [35]. This landslide presents a significant case study due to its potential to threaten the Baipaza Hydropower Station and the adjacent dam, located 5 km to the north. Covering an area of over five km², it lies along the right bank of the Vakhsh River, which originates in Southern Kyrgyzstan and flows westward through Northern Tajikistan before turning south toward the Western Pamir region [36,37]. The landslide has a long and complex history, marked by multiple movements and reactivations. The first documented reactivation occurred in 1968, partially obstructing the Vakhsh River. The volume of material involved in that event was estimated to be between 20 and 25 million m³ [2]. A second significant displacement event took place in May 1992, triggered by intense rainfall again damming the Vakhsh River. Following a 7.4-magnitude earthquake in the Hindu Kush region on 3 March 2002, the landslide began its third phase of movement, once more partially blocking the Vakhsh River [2]. The estimated volume of this event was 5–10 million m³ [38]. This event led to the formation of a lake, posing a threat to the hydropower station, with the water level rising by 7 m. Subsequently, the debris accumulated in the riverbed was removed using explosives, effectively mitigating the risk of flooding [39].

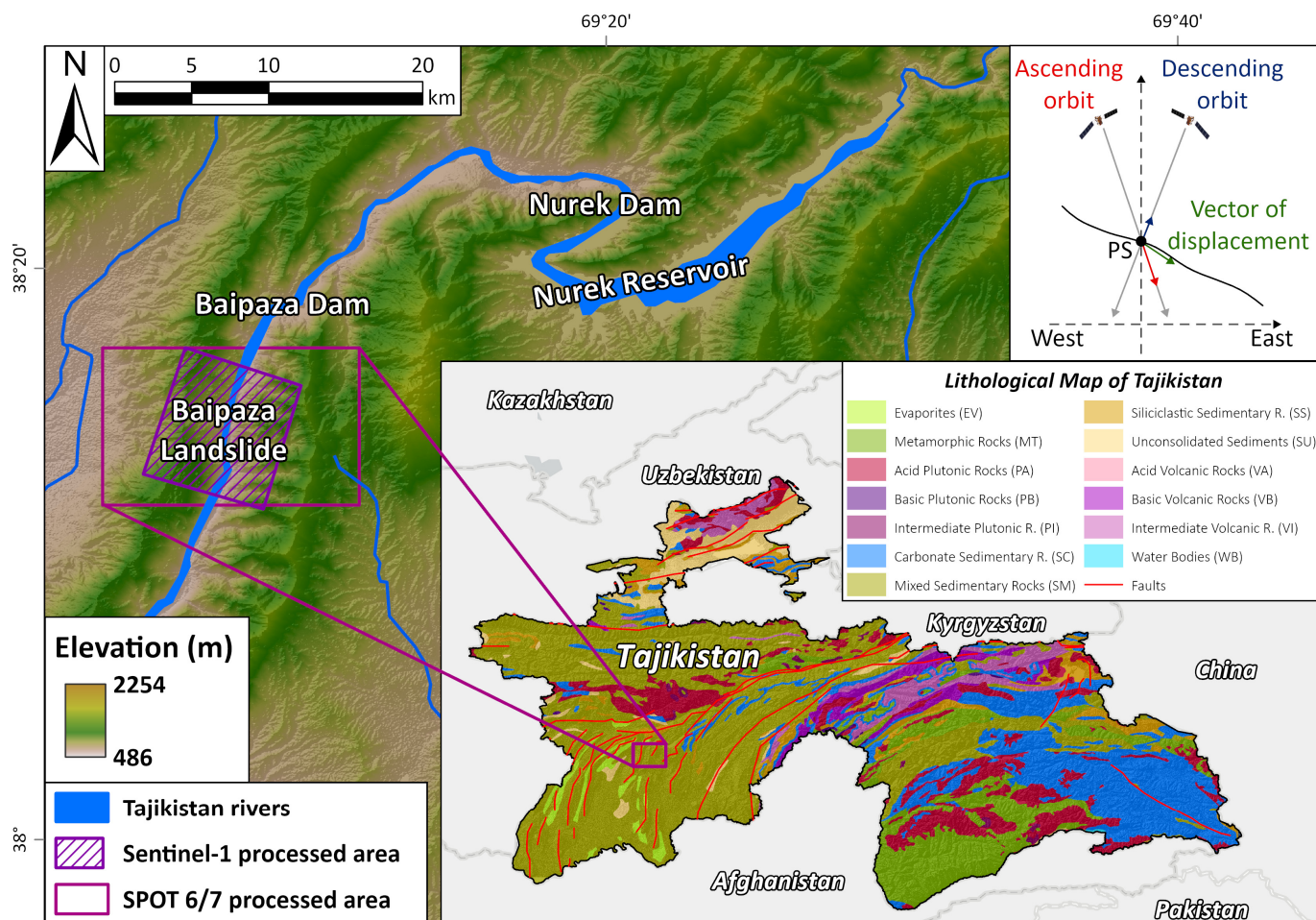


Figure 1. Baipaza Landslide location near the Baipaza dam in the Vakhsh River. This figure highlights the elevation model taken from the Terra Advanced Spaceborne Thermal Emission and Reflection Radiometer (ASTER) Global Digital Elevation Model (GDEM) Version 3 (ASTGTM) [40], and the lithological map of Tajikistan is taken from the GLiM database [41]. The angular relationship between the geometry of the landslide and the satellite acquisition LOS is illustrated in the upper right-hand quadrant of the figure.

In light of the history of sudden reactivations and the high potential for abrupt future movements due to the region's seismicity and other characteristics, Tajik authorities have implemented a mitigation program. The objective of this program is to prevent and reduce the risk of complete blockage of the Vakhsh River. Such a blockage would pose a significant challenge, as it could disrupt the power generation of the dam. The mitigation strategy involves stabilizing the landslide by removing material from the landslide's head and creating a series of benches in the head scarp area. Additionally, open-trench drains are being installed in the upper part of the landslide to improve stability. The plan also includes removing landslide debris from the river channel to restore its capacity and ensure normal flow. To further facilitate disaster mitigation, a proposal has been made to construct a bypass tunnel through the steep left bank of the Vakhsh River [38].

3. Materials and Methods

In order to enhance the comprehension of Baipaza landslide behavior between 2014 and 2020, a remote-sensing analysis was performed, utilizing two distinct image sets acquired by Sentinel-1 SAR and Sentinel-2 optical satellites. The Sentinel-1 SAR images were processed using advanced radar interferometry (InSAR) techniques in conjunction with Principal Component Analysis (PCA). The results obtained from the remote-sensing

techniques were subsequently used for the image interpretation of the landslide employing a high-resolution elevation model taken from the Terra Advanced Spaceborne Thermal Emission and Reflection Radiometer (ASTER) Global Digital Elevation Model (GDEM) Version 3 (ASTGTM) [40]. A flowchart detailing the utilized techniques is shown in Figure 2.

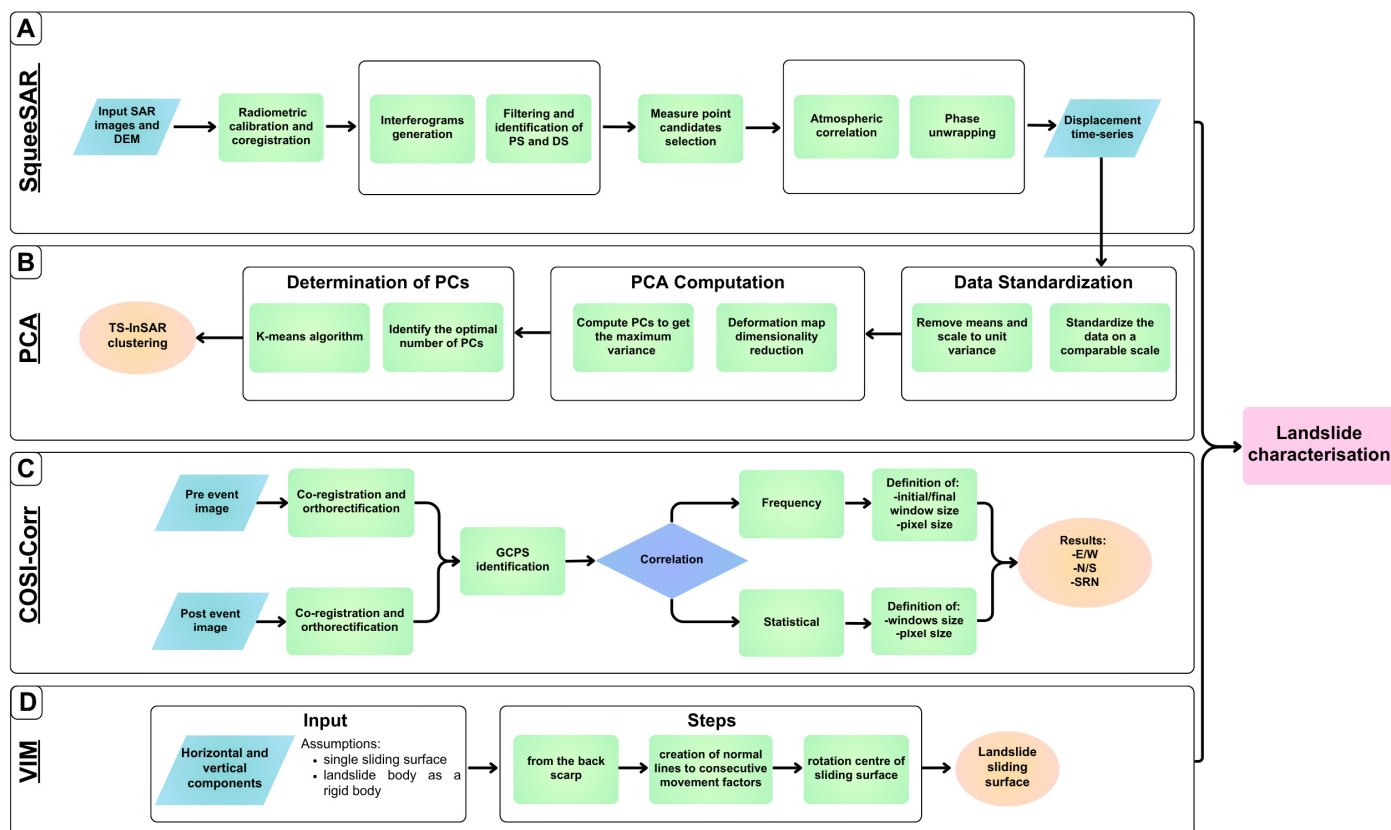


Figure 2. Simplified flowchart of the three techniques applied in the work: SqueeSAR (A), Principal Component Analysis (B), COSI-Corr (C), and Vector Inclusion Method (D). The outcomes of these analyses are used for the landslide characterization.

3.1. Multi-Interferometric Analysis of Radar Images

The InSAR has become a high-performance technique for measuring ground deformation induced by various geophysical phenomena. It analyzes radar signals from satellites to detect and measure changes on the Earth's surface. Over the years, numerous InSAR techniques have been developed to process satellite radar data. Multitemporal InSAR (MT-InSAR) approaches, such as Permanent Scatterer Interferometry (PSI) [42] and Small Baseline Subset (SBAS) [24], are used to analyze long series of SAR imagery and produce time series of displacement. Building from these two main algorithms, many different techniques have emerged, including CT-InSAR [43], StamPS [44], and SqueeSAR [23]. Despite the variety and individual differences of these approaches, they share a common principle: by comparing phase shifts between a series of radar images acquired over time, MT-InSAR can accurately measure the displacement of targets ranging from a few millimeters to tens of centimeters per year. Since the 1990s, the application of InSAR techniques has evolved from a specialized research area [45,46] to a practical tool extensively used in landslide studies [47–50]. The use of interferometric applications in the past two decades has been significantly advanced by the increased availability of satellite platforms equipped with microwave radar sensors operating at C-band (5–6 GHz, 5.6 cm wavelength), X-band (8–12 GHz, 3.1 cm wavelength), and L-band (1–2 GHz, 23.6 cm wavelength) level. All SAR satellites share the characteristic of acquiring images at a specific angle called the

line of sight (LOS). The LOS angle is subject to variation depending on the satellite and the acquisition mode, typically ranging from 15 to 50 degrees from the vertical direction. MT-InSAR has proven highly valuable for the remote detection of landslides, offering insights into different stages of landslide events [51]. It serves as a supporting tool for various applications, including mapping deforming slopes [52], modeling slope instabilities [53], characterizing landslide mechanisms, monitoring individual events [54], and zoning landslide sectors with distinct velocities and behaviors [55]. This technique allows for the mapping of landslides without requiring precise prior knowledge of their locations and is particularly advantageous for locating and studying landslides in remote or mountainous regions, where ground-based instruments may be impractical or inaccessible [56].

The InSAR data are subject to geometric distortions resulting from the side-looking acquisition geometry of the SAR sensor [57]. In the literature, the most critical distortions discussed are layover [58] and shadow [57], which occur predominantly in mountainous or steeply sloped areas. The layover distortion occurs when the radar signal reflected from the uppermost point of a terrain feature returns to the sensor ahead of the signal from the base, thereby resulting in a reversal of the anticipated spatial sequence and a compression of features along the radar line of sight [58]. Conversely, shadowing occurs when a steep terrain slope faces away from the sensor, thereby preventing radar illumination and resulting in areas devoid of backscatter information [57]. Consequently, these distortions can potentially compromise the accuracy of InSAR deformation measurements. The identification of such areas is achieved by generating layover and shadow masks through the analysis of local terrain geometry derived from a DEM (see Appendix A, Figure A1E–H) combined with sensor acquisition parameters, the incidence angle, and the azimuth direction. Table 1 presents the information and parameters of the SAR dataset exploited in this study for the implementation of the SqueeSAR approach. The InSAR measurements acquired from ascending and descending satellite geometries have been found to yield the LOS displacement velocities, which represent the component of ground displacement along the radar sensor’s look direction. The measurements can be decomposed to retrieve the vertical and horizontal components of ground displacement velocities through the inversion of a linear system relating the LOS versors and angles (see Table 1) to the vertical and horizontal components [57]. Subsequent to the acquisition of the vertical and horizontal components, the displacement velocity along the steepest slope direction of the terrain (V_{slope}) can be calculated by projecting the 2D displacement versors along the slope versors, derived from a DEM. The V_{slope} provides a meaningful parameter for assessing slope stability, especially in landslide-prone regions [59].

Table 1. The Sentinel-1 dataset is employed in the SqueeSAR process.

SAR imagery	SqueeSAR	
	Sentinel-1A	
Band	C	
Acquisition geometry	Ascending	Descending
Satellite track	71	78
Sensor mode	IW	IW
Number of scenes	147	142
Time range	10 October 2014–2 October 2020	23 October 2014–3 October 2020
Line-of-sight angle (θ)	40.55°	44.88°
Line-of-sight angle (δ)	9.98°	9.24°
Line-of-sight versors (V)	0.76	0.709
Line-of-sight versors (N)	−0.113	−0.113
Line-of-sight versors (E)	−0.64	0.696

Principal Component Analysis of Time Series

The majority of studies that have been conducted with the aim of mapping and characterizing ground motion have mainly relied on the average displacement rate obtained by fitting a linear regression model to the entire time-series InSAR (TS-InSAR) dataset [60]. However, only a limited number of methods have been evaluated for the purpose of detecting and classifying displacement signals from individual time series of ground deformation [61].

The procedure comprises three primary steps that have been developed within a Python 3.12.7 environment (Figure 2B) [62]: (i) The first step is the standardization of the TS-InSAR data to a comparative scale by eliminating the mean and scaling to unit variance. This step ensures that each feature contributes equally to the analysis, preventing bias in the PCA. (ii) The second step, the extraction of Principal Components (PCs), is a process that aims to maximize the variance in the dataset. The PCA is employed to identify the dominant spatial and temporal deformation patterns within each TS-InSAR dataset without imposing any prior assumptions. (iii) The third step is the clustering applying the K-means algorithm. The K-means implemented in its standard Euclidean form is an unsupervised and scalable clustering method used to group unlabeled and sparse TS-InSAR time series into clusters with similar characteristics. The only required parameter is the number of clusters, which is automatically determined on the basis of the optimal number of retained PCs.

It is important to note that each measurement point (MP) is grouped into a cluster made of displacement time series sharing similar patterns, e.g., stable linear trend, linear displacement with positive velocity, displacement with positive acceleration, etc. The approach under consideration is capable of detecting and characterizing different motion patterns in local unstable areas.

3.2. Correlation of Optical Images Using COSI-Corr

The COSI-Corr methodology (Figure 2C) involves the comparison of two input images, acquired prior to and following the deformation event. Following the identification of stable areas through the use of Ground Control Points (GCPs), the software generates two displacement components for each image pair: the north–south (N/S) and east–west (E/W) displacement layers. These layers represent the horizontal components of surface movement and are used to analyze and quantify the deformation patterns across the scene. A quality parameter known as the signal/noise ratio (SNR) is also generated. Positive values for N/S displacement denote the north direction, while positive values for E/W displacement indicate the east direction.

The COSI-Corr approach employs two distinct types of correlators: the frequency correlator and the statistical correlator. The frequency one, based on the Fourier technique, is more precise and sensitive to noise, making it suitable for generating high-quality images. Conversely, the statistical correlator is a less sophisticated approach that is employed in the context of noisy images that have already undergone frequency correlator analysis but have not yielded satisfactory results [63].

In this study, the frequency correlation was employed as a methodological framework. The utilization of the aforementioned correlator results in the attainment of findings that are distinct in nature, corresponding to a variety of initial–final window size combinations. The frequency correlation procedure is carried out in two main steps. The first step involves a coarse estimation of the pixelwise displacement between two corresponding image patches. The window size should be at least twice the expected displacement, but, in practice, a larger ratio [31] is recommended, because the increase in the window size reduces noise and uncertainty. Subsequent to the estimation of the initial displacement, a secondary,

concluding correlation is performed for the purpose of retrieving the subpixel displacement. The processing of the images involved various combinations of initial–final window size values in pixels, ranging from 8–8-pixel to 128–128-pixel configurations. The choice of window size influenced the quality of image measurements. A smaller window size, such as the 8–8-pixel configuration, resulted in lower measurement qualities, introducing uncertainty in the analysis of landslide displacement due to random occurrence of low measurement qualities, but providing more detailed information. It is more appropriate in small areas or applied to small landslides because the background noise could less influence the measurement. Conversely, increasing the window sizes, up to the 128–128-pixel initial–final window, led to clearer spatial patterns by minimizing background noise. The combination of elevated windows and expansive areas is more frequently documented in the literature, as it is particularly well-suited for large displacements. This enhancement allowed for a more accurate depiction of the landslide’s profile and shape. Moreover, it is possible to determine the pixel size, which contributes to enhanced spatial resolution of the results.

In the COSI-Corr investigation in the analysis, the images were processed using the 128–64-pixel combination, as it was determined to be the optimal combination for this case to characterize and study the movement of the landslide in terms of details and measurement quality of the results. It is evident that lower pixel combinations introduce uncertainty into the analysis due to the high dimensionality of the landslide. Conversely, higher combinations exhibit a paucity of detailed information, which does not highlight or display the specific landslide displacement. Table 2 presents the information of the Sentinel-2 images and parameters exploited in this study for the implementation of the COSI-Corr method. In Appendix A (Figure A1I,J) are illustrated the two Sentinel-2 scenes used.

Table 2. The Sentinel-2 dataset and the parameters employed in the COSI-Corr process.

COSI-Corr	
Optical imagery	Sentinel-2A
Band	Multispectral 13 bands
Number of scenes	2
Primary imagery	26 July 2016
Secondary imagery	29 August 2022
Initial window size	128 pixels
Final window size	64 pixels
Step	2 pixels

3.3. Vector Inclination Method

The Vector Inclination Method (VIM) was employed to conduct a comprehensive analysis of the Baipaza landslide, with the objective of gaining insights into the characteristics of the sliding surface. This approach was undertaken in accordance with the methodology outlined in [64], and subsequently validated through the utilization of InSAR data by [65]. The VIM utilizes the horizontal and vertical ground movement components along a longitudinal section, operating under the assumption that the surface movement reflects the sliding surface’s geometry. The application of VIM is contingent upon two fundamental conditions: the presence of a single sliding surface and the assumption that the landslide body behaves as a rigid body. Although not obligatory, the density of MPs has been demonstrated to enhance the outcomes, particularly in the context of shallow landslides [65]. The procedure involves creating a landslide section that is the intersection of the MPs. The determination of normal lines to consecutive movement vectors is initiated from the back scarp. The intersection of these lines demarcates the rotation center of the sliding surface between the given vectors. This process is repeated for all vectors.

A detailed description of the practical procedure is given by [66], who firstly proposed a geometrical solution to the original method by [64]. While the method yields a series of circular sections, the results can also represent planar shapes, as they may be circular sectors with large curvature radii.

In the present study, the vertical and horizontal components of the Sentinel-1 dataset were utilized, under the supposition that the movement direction on the horizontal plane is parallel to the slope. Although the VIM generally benefits from calibration with independent landslide-thickness data (e.g., inclinometric measurements), in this case, the VIM offers a practical method of acquiring preliminary information regarding the geometry and depth of the sliding surface.

4. Results

4.1. InSAR Results

The results obtained from the SqueeSAR processing of the available Sentinel-1 images are presented as average displacement rates along the ascending and descending LOS, respectively, in Figure 3A,B. The decomposed displacement in the horizontal and vertical components is presented as average rates, respectively, in Figure 3C,D. Finally, in Figure 3E, the mean rates are presented along the steepest slope, which is designated as the V_{slope} .

The mean LOS velocity rates, measured in millimeters per year (mm/year), are represented by positive values (shown in blue), which indicate movement toward the satellite, while negative values (shown in red) indicate movement away from the satellite. The context of the components velocity rates: Positive values correspond to eastward motion, while negative values correspond to westward motion. The total number of MPs obtained across the entire study area is 83,499 for the ascending geometry, 78,759 for the descending geometry, and 11,402 for the horizontal and vertical components. In the landslide area specifically, 5950 MPs are available for the ascending geometry, 5111 for the descending geometry, and 714 for the horizontal and vertical components, with a maximum density of 1045 MPs/km² observed in the ascending geometry data. The accuracy of InSAR deformation measurements is evaluated by the illustration of the layover and shadowing mask for the entire area of the Baipaza landslide, as demonstrated in Appendix A. The landslide's eastward aspect results in significant shadowing distortion in the ascending geometry, as evidenced by the reduced density of MPs over the landslide in comparison to the descending geometry. The landslide area exhibits notably high deformation rates, with peak values of -141.1 ± 0.4 mm/year in the ascending geometry and 240.2 ± 0.6 mm/year in the descending geometry. The maximum deformation rate in the horizontal component is 246.9 ± 0.6 mm/year (eastward), while the vertical component's deformation rate ranges from -65.4 ± 0.6 , in the area close to the scarp, to 114.7 ± 0.7 mm/year. The maximum deformation rate in the V_{slope} component is 114.7 ± 0.7 mm/year. The lower portion of the landslide exhibits a gradual shift from negative (downward) to positive (upward) vertical displacements. The distribution of deformation components is indicative of a downhill movement and a substantial horizontal velocity. This suggests the presence of a sliding surface with a rotational geometry.

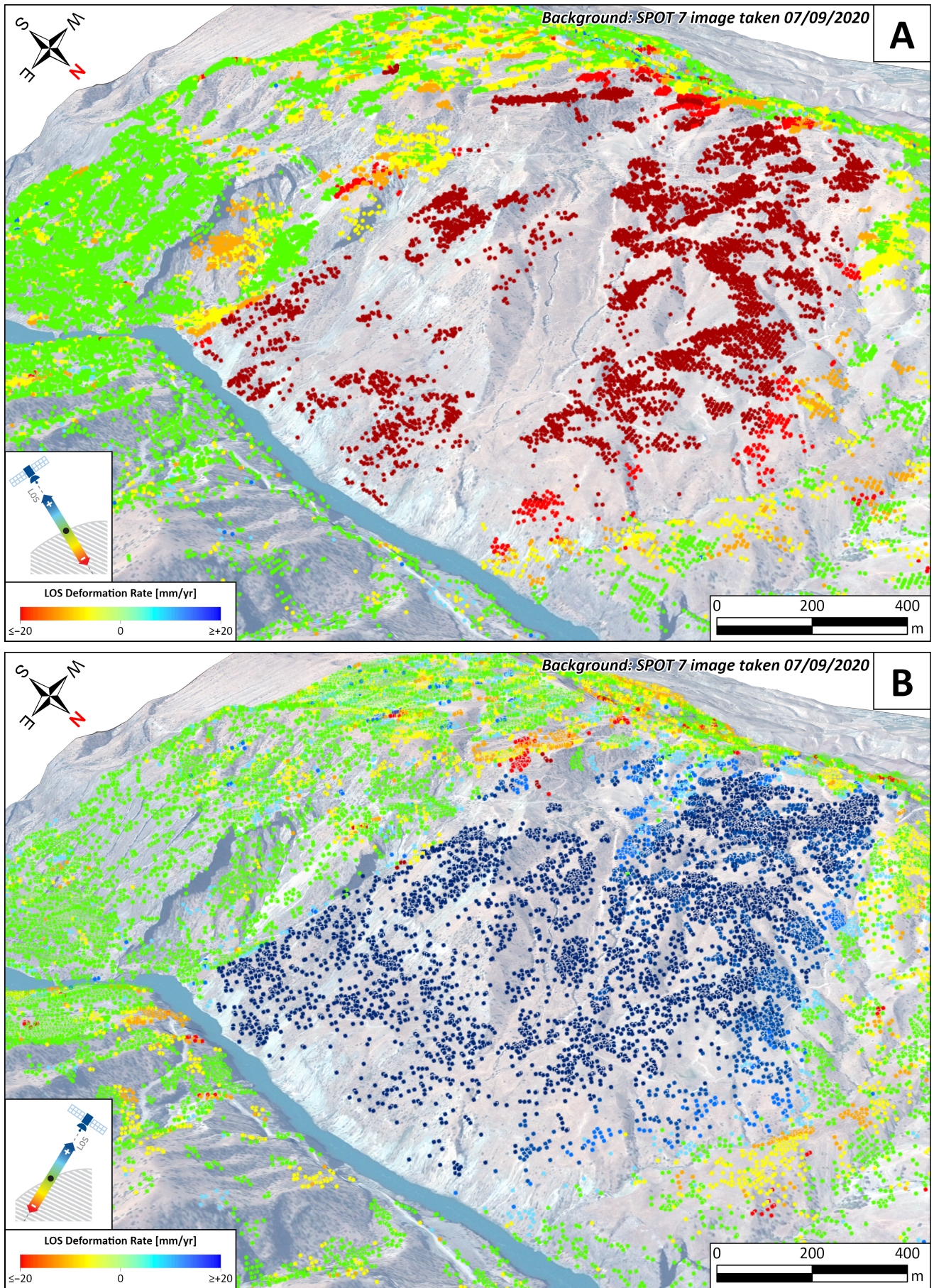


Figure 3. Cont.

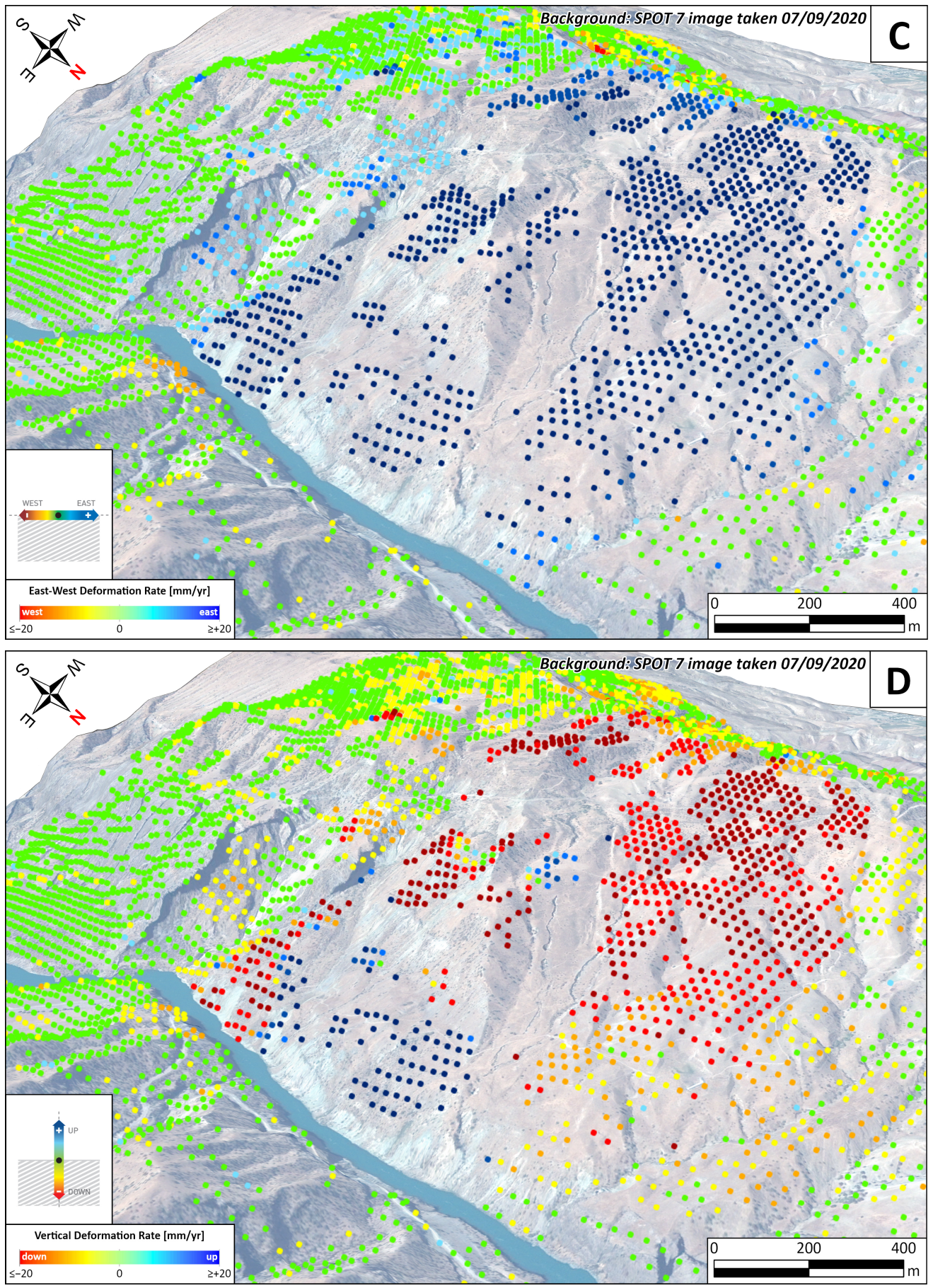


Figure 3. Cont.

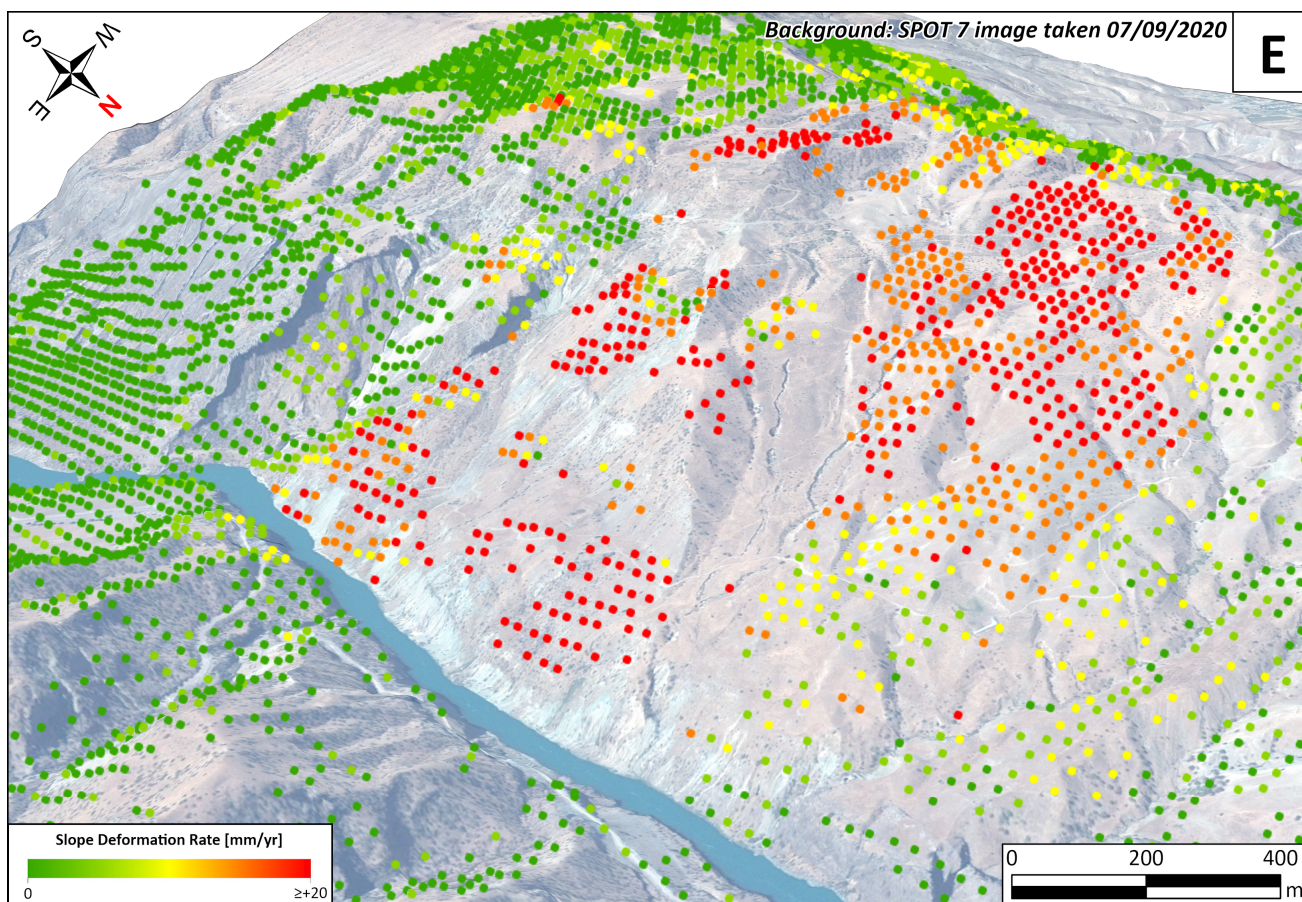


Figure 3. Representation of the ground deformation for both geometries, (A) ascending and (B) descending, and for all components, (C) horizontal, (D) vertical, and (E) along the slope.

The landslide displays a range of velocity patterns, as evidenced by the PCA and TS-clustering was performed using a K-means algorithm, applied to the ascending and descending geometries (Figure 4A,B) and to the horizontal and vertical components (Figure 4C,D), respectively. The analysis of displacement time series provides further confirmation of the variability in landslide kinematics, as indicated by distinct spatial deformation patterns. The investigation's findings indicate the presence of MPs classified into various clusters. As illustrated in Figure 4, the subsequent segment of each component is designated to exhibit the plots of the time-series displacement for each cluster. The red curve serves as a visual representation of the 50th percentile (median) of displacement values within the cluster over time. This indicates the central tendency or typical behavior of the points in that cluster. The grey-shaded area, delineated by the 10th and 90th percentiles, illustrates the variability of displacement values, capturing the range encompassing 80% of the data.

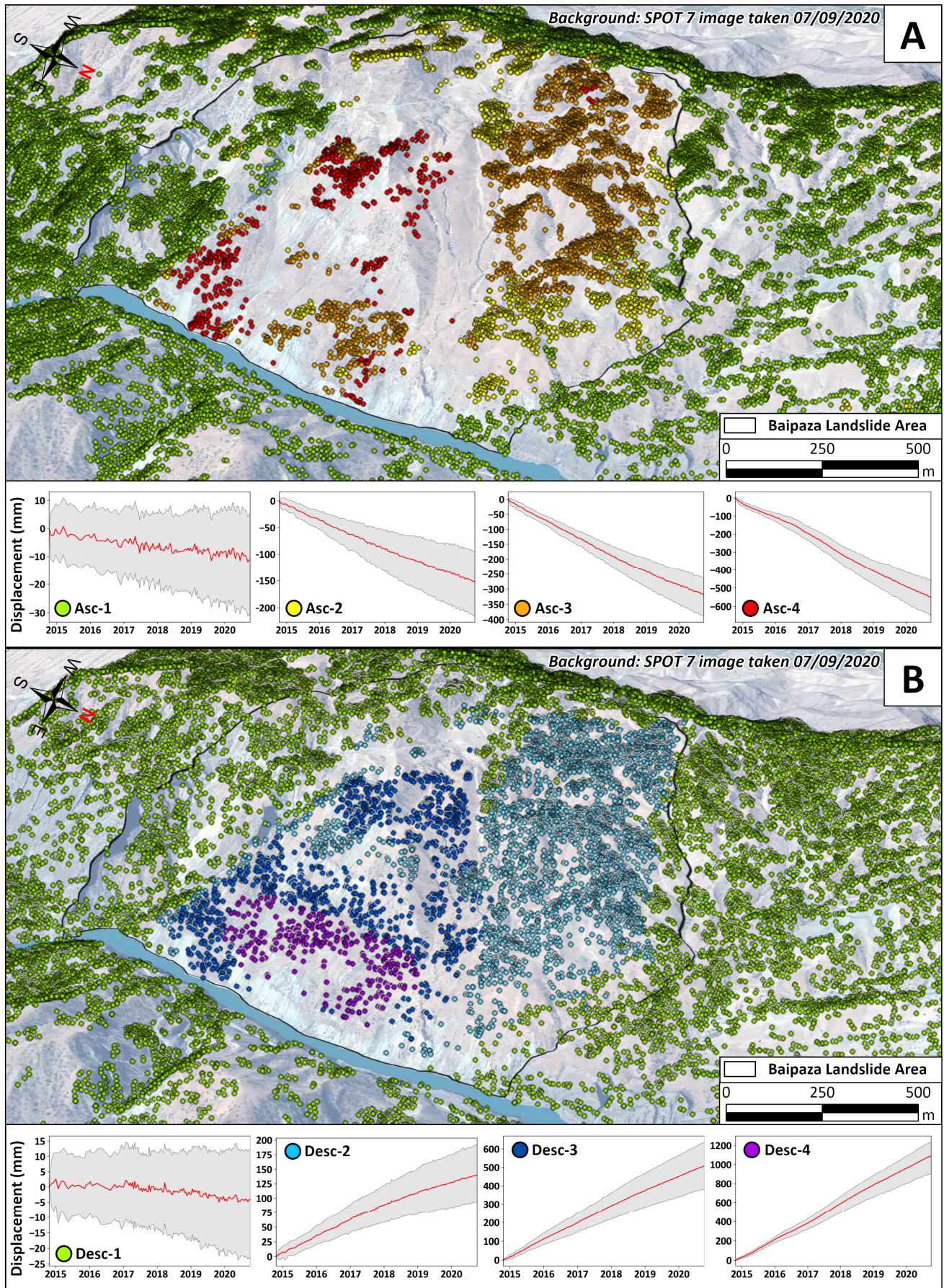


Figure 4. Cont.

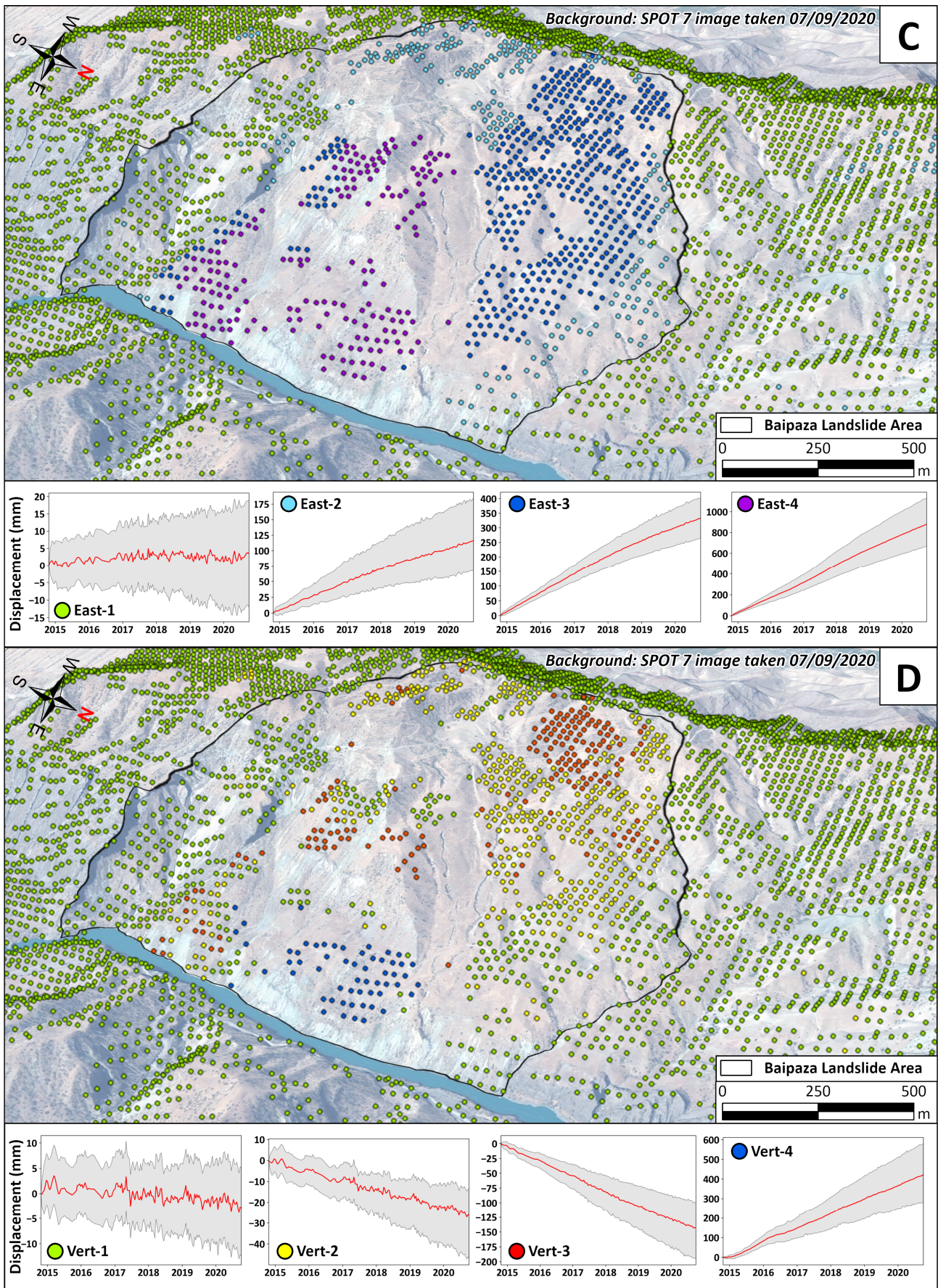


Figure 4. Map of the distribution of the features classified according to the PCA and TS-clustering analysis: (A) ascending, (B) descending, (C) horizontal, and (D) vertical. In the lower section of each

component, the displacement time-series graphs are displayed for each cluster. The red curve provides a visual representation of the 50th percentile (median) of displacement values within the cluster over time. The grey-shaded area, delineated by the 10th and 90th percentiles, illustrates the variability of displacement values, capturing the range encompassing 80% of the data.

In the context of the ascending geometry (Figure 4A), four distinct clusters were identified, each characterized by negative displacement (movement away from the satellite). The “Asc-1” cluster represents areas with negligible deformation, showing a cumulative displacement between 10 mm and -30 mm over six years (from October 2014 to October 2020). The other three clusters indicate areas with ongoing deformation: “Asc-2”, with a maximum cumulative displacement of -200 mm; “Asc-3”, with -400 mm; and “Asc-4”, with -600 mm. Similarly, the PCA of the descending geometry (Figure 4B) revealed the presence of four distinct clusters, with positive displacement values (movement towards the satellite). The “Desc-1” cluster represents areas with minimal deformation, with a maximum cumulative displacement between -25 mm and 15 mm. The “Desc-2” cluster shows a maximum cumulative displacement of 200 mm, “Desc-3” of 600 mm, and “Desc-4” of 1200 mm. Despite this variability, the time series for both ascending and descending datasets within the Baipaza landslide exhibit linear trends without seasonal fluctuations. The PCA of the horizontal dataset (Figure 4C) also demonstrates the presence of four distinct clusters, all exhibiting positive displacement, characterized by an eastward movement. The “East-1” cluster denotes areas with negligible horizontal deformation, having a maximum cumulative displacement between -15 mm and 20 mm. The other three clusters indicate areas with deformation: “East-2”, with a maximum cumulative displacement of 175 mm; “East-3”, with 400 mm; and “East-4”, with 1000 mm. In contrast, the four clusters for the vertical dataset (Figure 4D) are significantly divergent. The “Vert-1” cluster has a maximum cumulative displacement of -25 mm, generally representing areas with negligible vertical displacement. The “Vert-2” cluster indicates vertical displacements up to -140 mm, and “Vert-3” up to -250 mm. Conversely, the “Vert-4” cluster exhibits positive vertical displacements, reaching values up to 600 mm. As with the other components, the deformation trends for the horizontal and vertical components are linear and free of seasonality. Meanwhile, the PCA and TS-clustering results might seem inconclusive due to only linear movements being observed, potentially overlooking more complex deformation patterns. Nonetheless, the PCA and TS-clustering allow for the statistical and unsupervised identification of distinct sectors within the Baipaza landslide, each characterized by different deformation patterns and velocities. Following a thorough examination of the time-series analysis results, it was determined that optical images should be utilized to gather data on landslide deformation in areas where InSAR data were unavailable due to geometric-distortion issues.

4.2. COSI-Corr Results

The result of the analysis of the optical images acquired by Sentinel-2 and processed using the COSI-Corr algorithm with the 128-64-pixel combination is presented in Figure 5. The result was subjected to a non-local mean filter, which exploited the signal-to-noise ratio, one of the outputs of the processing. This methodological approach permitted the elimination of the excessively noisy displacement component, which was primarily caused by disparities in shadowing between the two selected scenes. In Figure 5 presents the results of both the COSI-Corr and InSAR TS-clustering for the east–west component, which is the primary component of landslide displacement. In consideration of the approximate six-year time baseline between the two Sentinel-2 scenes (26 July 2016–29 August 2022), it is reasonable to consider that the COSI-Corr displacement measurements are less precise than the more accurate InSAR measurements. The COSI-Corr measurement is subjected to

decorrelation due to a phenomenon that is primarily attributable to seasonal variations or the proliferation of vegetation. The hypothesis is substantiated by the standard deviation of the COSI-Corr displacement measurements of 0.81 m, which indicates the margin of error in the displacement measurements. The signal-to-noise ratio (SNR), a measure of correlation quality, is also computed using the COSI-Corr function. It is evident that outcomes exhibiting enhanced dependability are associated with SNR values that approximate unity [67]. The mean value of the signal-to-noise ratio (SNR) over the Baipaza landslide, as determined by the COSI-Corr outcome, is approximately 0.98, indicating a high degree of reliability and consistency (see the SNR map in Appendix A, Figure A1K). However, the most notable aspect is the increased spatial coverage of the deformation, which provides additional information about the displacement of the landslide.

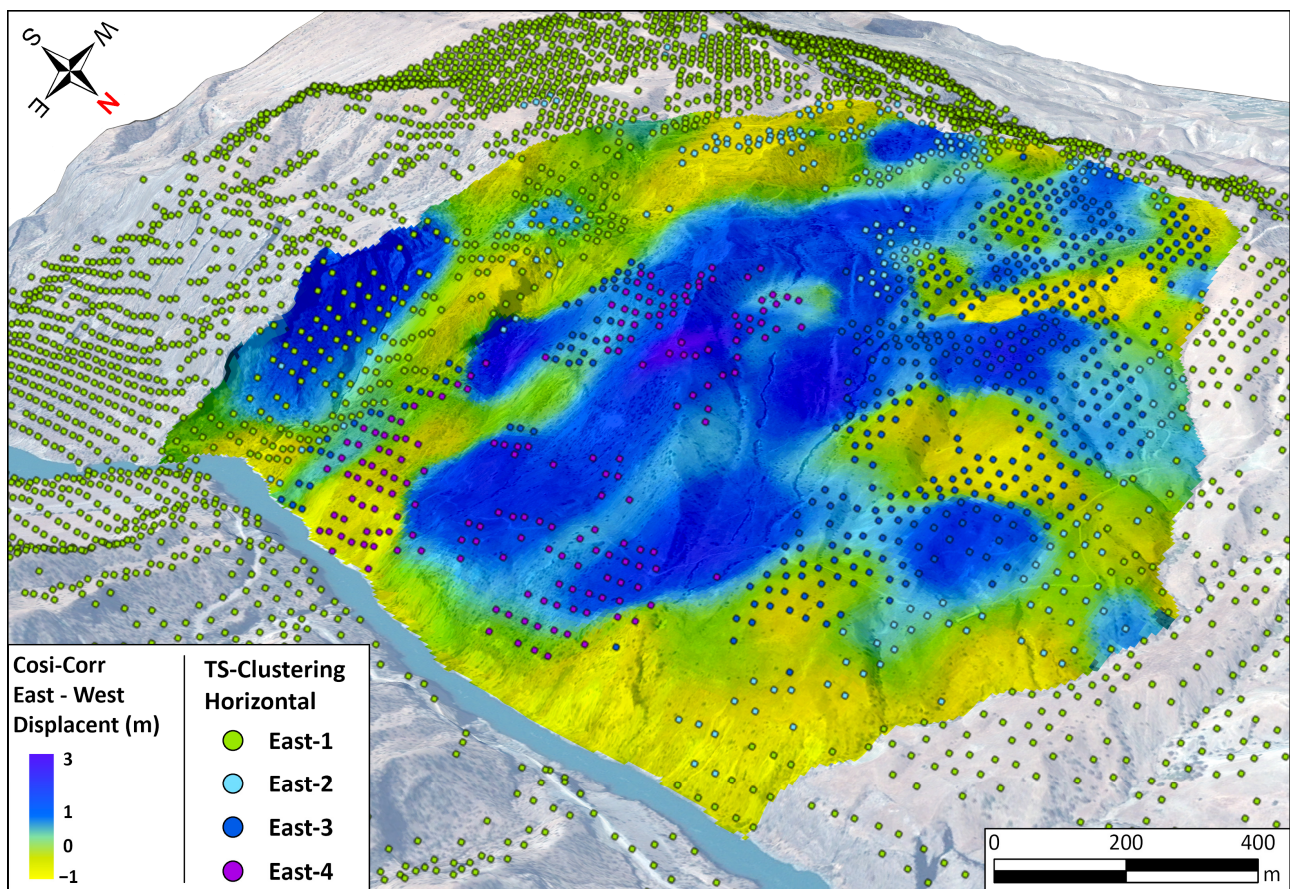


Figure 5. COSI-Corr result of the Sentinel-2 images for the E-W component. Positive (blue) values indicate eastward movements, and negative (yellow) represent westward movements.

The results obtained from the analysis indicate that the area exhibiting the greatest deformation is located in the central portion of the landslide, as indicated by the blue-to-violet tones. However, notable discrepancies are observed between the two results. Firstly, in the southernmost portion of the landslide, COSI-Corr identifies a significant eastward displacement, whereas InSAR indicates negligible deformation. The second area of discrepancy is observed in the northern portion of the landslide, where COSI-Corr identifies multiple regions exhibiting intense deformation (represented by blue tones) interspersed with areas displaying significantly lower deformation. In contrast, InSAR detects widespread intense deformation, exhibiting a single deformation trend across the majority of the area. Finally, it should be noted that the areas within the COSI-Corr result display negative displacement values (represented by yellow tones), predominantly concentrated along the scarps adjacent to the Vakhsh River.

4.3. Vector Inclination Method Results

To further analyze the landslide and gain insights into the sliding surface, the Vector Inclination Method (VIM) was applied. To satisfy the assumption of a single sliding surface assumption, the cross-section was drawn near the northern boundary (Figure 6). The VIM results suggest a compound sliding surface with a linear, homogeneous sliding direction abruptly transitioning to a shallower surface near the landslide's foot, reaching a maximum depth of 400 m and a dip angle of approximately 26° (Figure 6). Assuming a similar depth and geometry across the landslide's width, it is possible to estimate a total volume of the order of magnitude of approximately 1 billion m^3 .

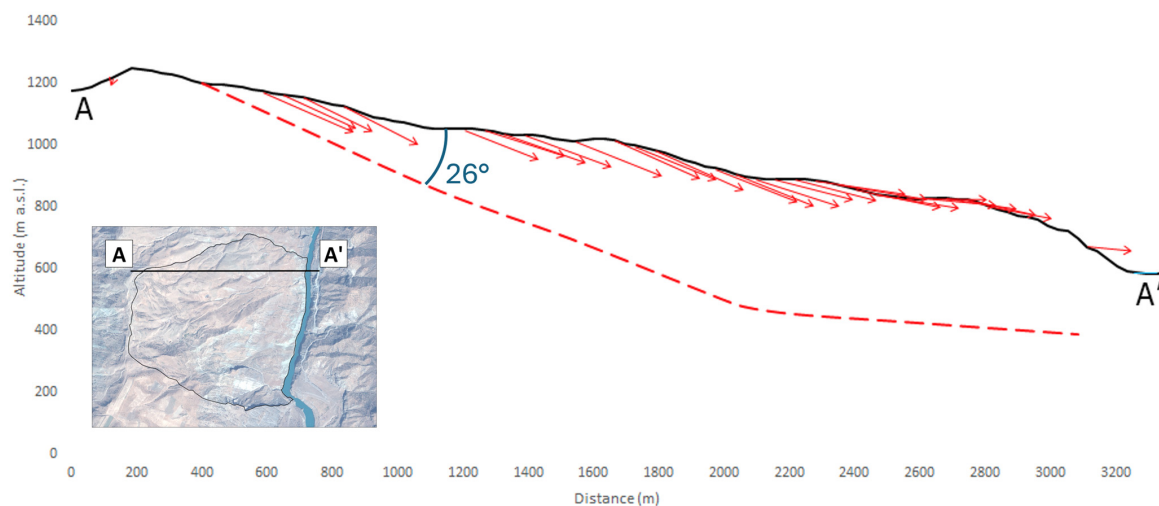


Figure 6. Reconstruction of the sliding surface (red dotted line) of the right-bank slide using the VIM along the A-A' cross-section. The red arrows indicate the displacement vectors of the MPs projected along the cross-section. In the inlay, the location of the cross-section is shown (black line).

5. Discussions

The objective of this study is to comprehensively utilize the capabilities of Sentinel-1 radar imagery and Sentinel-2 optical imagery to detect and quantify active movements within the Baipaza region of Tajikistan. The SqueeSAR algorithm, applied to Sentinel-1 radar images, and the COSI-Corr algorithm, applied to Sentinel-2 optical images, successfully identified a range of active movements. This integrated approach facilitated the precise mapping of landslide boundaries and the identification of distinct sectors with varying deformation patterns (Figure 7). This delineation was achieved through a multifaceted methodology incorporating radar interpretation, remote-sensing data, and geomorphological analysis. Specifically, the landslide's boundaries and internal structure were determined by combining InSAR-derived velocity fields, optical image correlation, and high-resolution topographic data from digital elevation models. This integration allowed for the differentiation of zones exhibiting differing kinematic behaviors, providing a more refined understanding of the landslide's evolution. In order to achieve a comprehensive understanding of the landslide, it was crucial to accurately delineate both the scarp and the landslide body for each sector. The first identified sector, designated "Baipaza A" (illustrated in yellow tone in Figure 7), covers the entire landslide body and exhibits characteristics of an ancient landslide that is still active. However, due to the effects of long-term erosion, the mapping of the original scarps presented significant challenges. The integration of displacement data from both InSAR and COSI-Corr provided key information on the spatial distribution of ground deformation, which resulted in being around 5.69 km^2 .

The classification of additional sectors was made possible by identifying subsequent reactivation events. Data for these sectors will be discussed according to their stratigraphic

and temporal sequence of activation (Figure 7). “Baipaza B” (in green) and “Baipaza C” (in tan) are daughter landslides of “Baipaza A”. Delineation of their scarps and landslide bodies involved the integration of high-resolution topographic analyses and remote-sensing data. InSAR analysis revealed average east–west velocities of 57 mm/year for “Baipaza B” and 88 mm/year for “Baipaza C”.

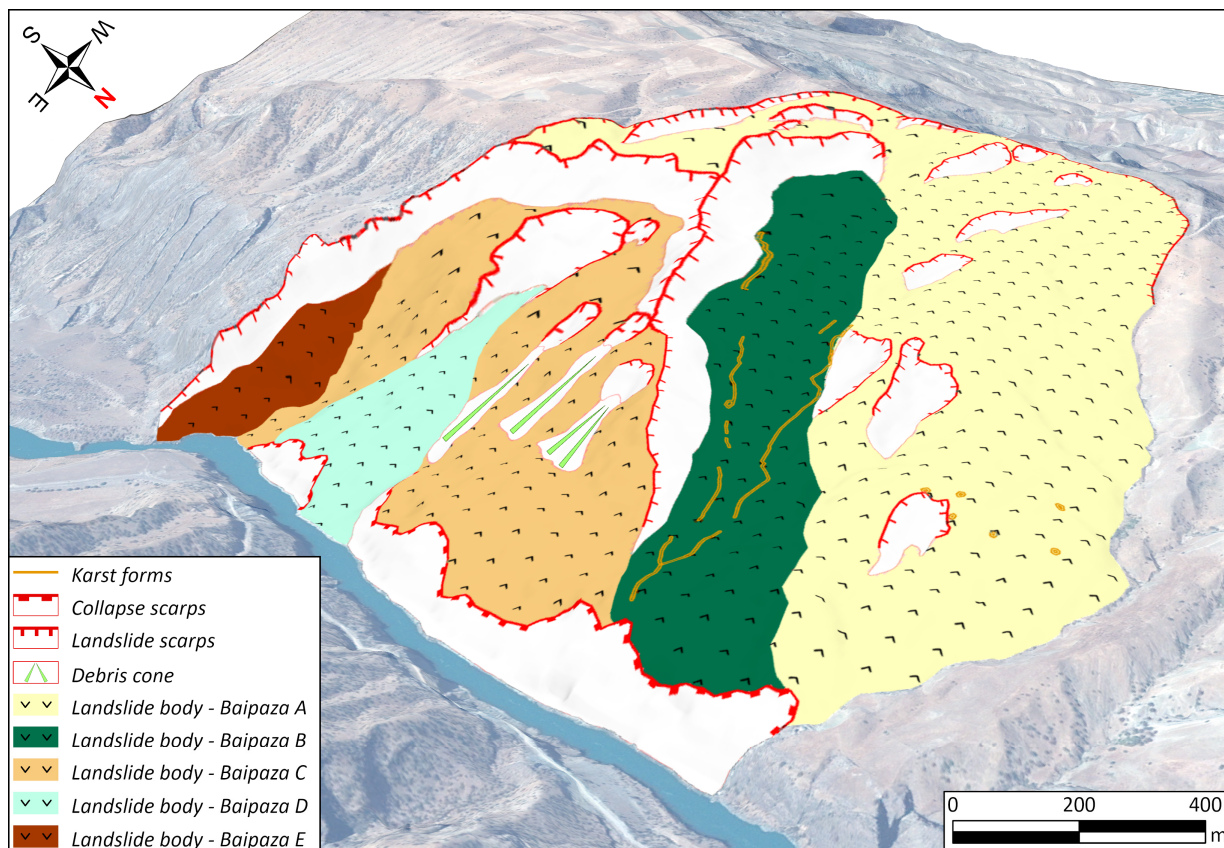


Figure 7. Mapping of the four different landslides affecting the study area, carried out through the exploitation of radar and optical satellite data.

“Baipaza D” (in light blue) and “Baipaza E” (in brown), the most recently reactivated sectors, display different kinematic behaviors. InSAR analysis indicates that “Baipaza D” has the highest average displacement velocity of 126 mm/year. The “Baipaza E” landslide body is situated at the base of a steep, north-oriented scarp, which creates considerable shadowing, thus limiting the effectiveness of InSAR measurements. Although the COSI-Corr technique proved to be effective in detecting ground deformation in this sector, the obtained rates may be overestimated due to shadow interference with the optical correlation process.

A series of minor and superficial phenomena are apparent in Figure 7. The northernmost sector shows numerous smaller scarps directly on the landslide “Baipaza A”. Consequently, these scarps are unrelated to the later reactivations in the southernmost area. Furthermore, three debris cones are identified above the “Baipaza C” landslide. The presence of ridge doubling indicates multiple reactivations of the landslide. Notably, karst forms, shown in orange on the map, are also present in the northern part, which is consistent with the carbonate rock composition of the area (Figure 1). These karst features can be categorized into linear forms, including karst rivers with both surface and subsurface courses, and punctual forms, such as dolines.

The Vector Inclusion Method (VIM) was used to characterize the landslide sliding surface. The results of this study suggest the presence of a compound sliding surface

characterized by a linear, homogeneous sliding direction. The maximum depth recorded was 400 m, with an approximate dip angle of 26° , and the total estimated volume was of the order of magnitude of approximately 1 billion m^3 . In the area surrounding the Baipaza landslide (Appendix A, Figure A1L), the presence of lithostratigraphic structures, such as flat irons and exposed geological strata, is observable. It was determined that the inclination of these layers exceeds that of the slope. The estimated inclination ranges from 30 to 35° . In consideration of the aforementioned information, it is reasonable to conclude that the landslide volume assessment is likely to be an underestimation of the actual volume.

The combination of these observations, particularly the presence of double crest lines and scarp [68,69], and the high-relief slope of the area [70], allows for the formulation of a hypothesis regarding the classification of the Baipaza landslide as an extensive, deep-seated gravity slope deformation (DSGSD).

Our analysis revealed notable discrepancies between the InSAR and the COSI-Corr techniques. InSAR, with its well-established processing methodologies and higher temporal resolution, reliably captured the deformation rates across different sectors of the landslide. Conversely, the interpretation of the COSI-Corr results proved more challenging due to the utilization of only two optical images acquired approximately six years apart. This extended interval introduces considerable uncertainty into absolute displacement measurements, contingent on factors such as image quality and ground conditions. However, COSI-Corr identified phenomena not seen in the InSAR data. The initial hypothesis posited that the negative (westward) displacements detected in the COSI-Corr analysis (see yellow tones in Figure 5) were artifacts caused by shadowing, seasonal changes in illumination, or color shifts due to atmospheric or surface conditions. These artifacts are particularly prevalent in areas with steep topography, where geometric distortions can degrade the optical correlation. Furthermore, the presence of snow covers in high-altitude regions has the potential to obscure surface textures and compromise the accuracy of the correlation, particularly when one image is captured during a snow-covered season and the other during a snow-free period. Consequently, the Sentinel-2 images selected for the analysis were captured during the summer season. Despite these challenges, some of the westward displacements observed in COSI-Corr results align spatially with geomorphic features such as scarps of the landslide, particularly near the base of deposits where river erosion is active. The observed COSI-Corr displacement is potentially overestimated; it may be attributed to factors such as image decorrelation or projection effects.

The integration of both datasets provides complementary insights into the dynamics of the Baipaza landslide; however, a careful assessment of data limitations and potential sources of error remains essential for accurate interpretation. One of the primary limitations of this study is the lack of ground-based measurements, such as terrestrial laser scanning [71], GPS, or unmanned aerial vehicle (UAV) photogrammetry [72], which could provide an independent validation of satellite-derived displacement data. This limitation is primarily due to the remoteness and inaccessibility of the study area. Future research should aim to incorporate ground-based techniques to enhance the reliability and spatial resolution of the deformation analysis. Despite these constraints, the findings of this study offer valuable support to local authorities by providing a detailed understanding of landslide behavior and demonstrating the potential of remote-sensing techniques to continuously monitor the landslide.

6. Conclusions

The topographical complexity and seismic activity experienced by Tajikistan render the country particularly vulnerable to natural hazards, including earthquakes and floods. The geomorphological features of the region have been identified as a contributing factor

to the triggering of substantial and deep-seated landslides, such as the Baipaza landslide. The extant literature on this area is scant, with the majority of studies concentrating on the seismic-induced collapse that occurred in March 2002 following a 7.4 magnitude earthquake (see [2]). This event involved an estimated 5–10 million m³ of material, resulting in a partial blockage of the river and a notable increase in the dam's water level. The utilization of InSAR data, processed using the SqueeSAR technique and analyzed through the PCA, provided crucial information on the temporal evolution of deformation and facilitated the initial identification of different landslide sectors. The InSAR time series, covering the period from October 2014 to October 2020, exhibited a linear trend with a maximum rate of 246 ± 0.6 mm/year across the various Baipaza landslide sectors. Conversely, the COSI-Corr module, applied to Sentinel-2 optical images, yielded valuable spatial data related to the boundaries of the landslide sectors. Radar interpretation revealed the presence of five distinct landslide bodies and scarps, each corresponding to a different reactivation event (Figure 7). The geometry and depth of the sliding surface were estimated using the Vector Inclination Method (VIM) technique, which was applied to InSAR data. This analysis suggests a sliding surface depth of 400 m, with an approximate dip angle of 26°. The total estimated volume was of the order of magnitude of approximately 1 billion m³. The combination of these observations allows for the formulation of a hypothesis regarding the classification of the Baipaza landslide as an extensive deep-seated gravity slope deformation (DSGSD). This hypothesis is supported by the presence of double crest lines and scarp, as well as the high-relief slope of the area. The findings of this analysis are likely to be of significant value to local administrations, as they provide an exhaustive examination of volume estimation and the feasibility of leveraging comprehensive remote-sensing techniques to establish a continuous monitoring framework for landslide evolution.

Author Contributions: Conceptualization, F.P. and O.N.; methodology, F.P. and O.N.; formal analysis, F.P. and O.N.; resources, R.M. and S.F.; data curation, F.P. and O.N.; investigation, F.P. and O.N.; writing—original draft preparation, F.P., O.N., R.M., S.F. and E.I.; writing—review and editing, F.P.; visualization, F.P. and O.N.; supervision, F.R.; validation, E.I., R.M. and S.F.; project administration, F.R. All authors have read and agreed to the published version of the manuscript.

Funding: This research received no external funding.

Data Availability Statement: The data presented in this study are available on request from the corresponding author due to privacy reasons.

Conflicts of Interest: Authors Simone Fiaschi and Roberto Montalti were employed by the company TRE ALTAMIRA. The remaining authors declare that the research was conducted in the absence of any commercial or financial relationships that could be construed as a potential conflict of interest.

Abbreviations

The following abbreviations are used in this manuscript:

COSI-Corr	Co-Registration of Optically Sensed Images and Correlation
GCPs	Ground Control Points
InSAR	Interferometric Synthetic Aperture Radar
SBAS	Small BAseline Subset
PCA	Principal Component Analysis
PCs	Principal Components
MPs	measurement points
TS-InSAR	time-series InSAR

Appendix A

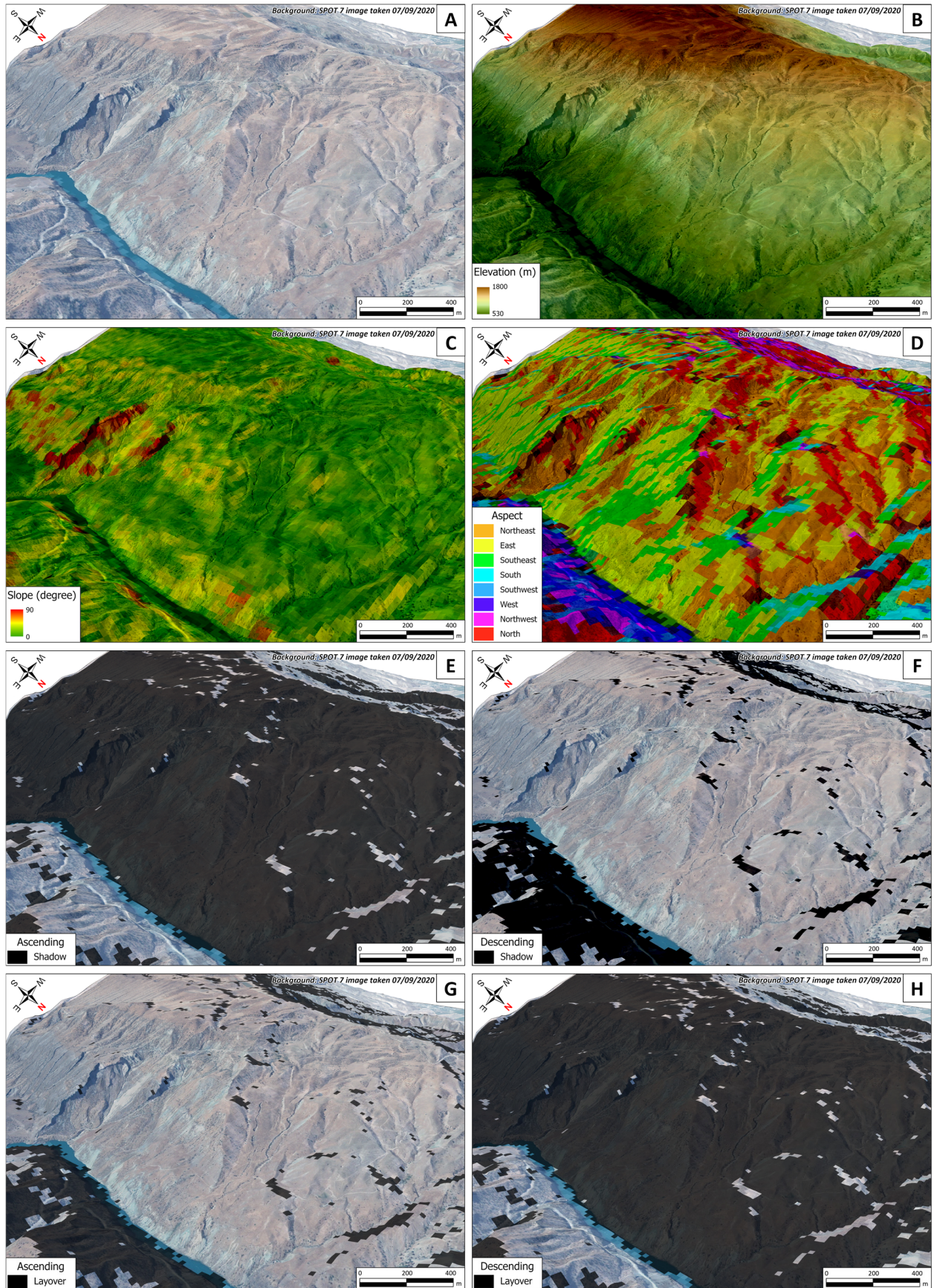


Figure A1. Cont.

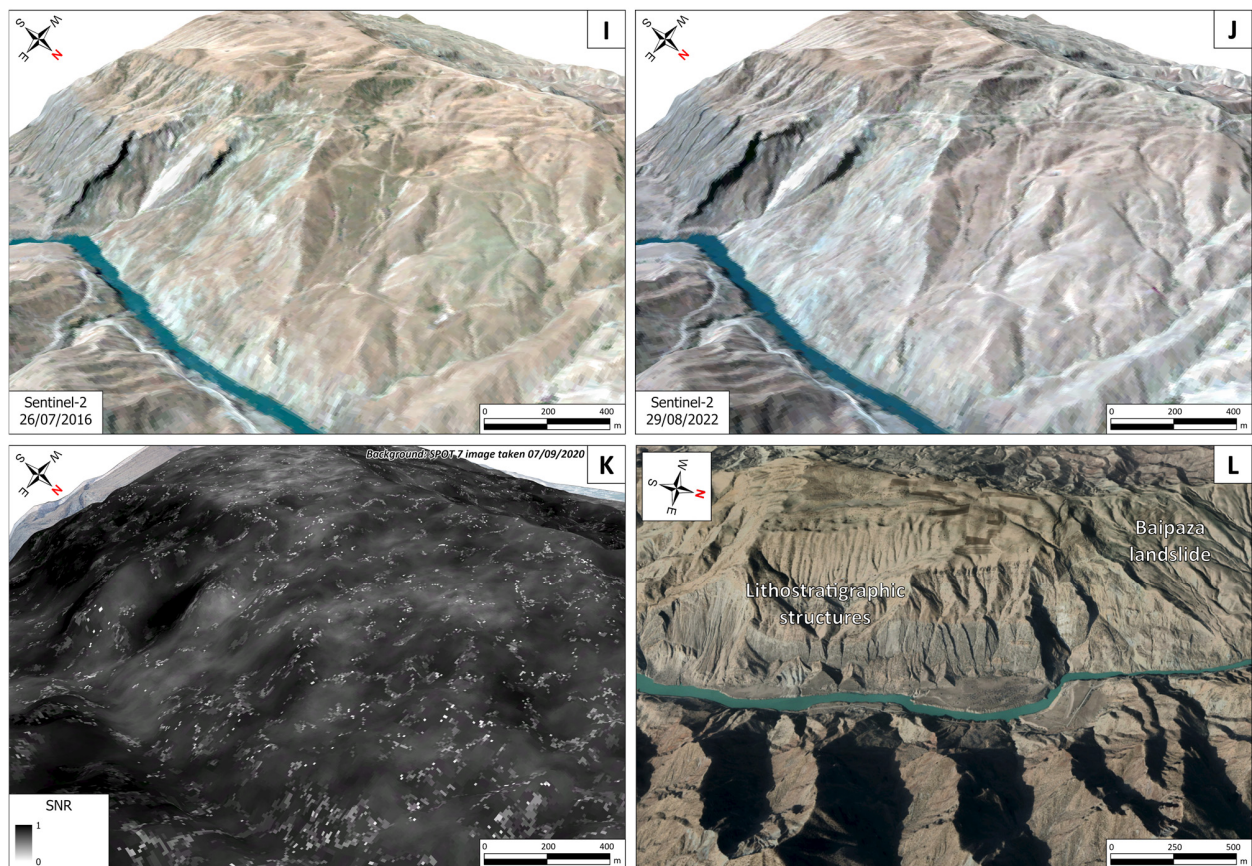


Figure A1. The representation of different spatial data used in this study. (A) High-quality RGB image (Red: B2—660 μm , Green: B1—560 μm , Blue: B0—485 μm); (B) the digital elevation model from the ASTER DEM; (C) slope; (D) aspect; (E) shadow mask of the ascending InSAR dataset; (F) shadow mask of the descending InSAR dataset; (G) layover mask of the ascending InSAR dataset; (H) layover mask of the descending InSAR dataset; (I) the Sentinel-2 acquisition in 26 July 2016; (J) the Sentinel-2 acquisition in 29 August 2022; (K) the SNR result from the COSI-Corr algorithm; (L) evidence of the lithostratigraphic structures in the area surrounding the Baipaza landslide, optical image from Google Earth Pro.

References

- Nadim, F.; Kjekstad, O.; Peduzzi, P.; Herold, C.; Jaedicke, C. Global landslide and avalanche hotspots. *Landslides* **2006**, *3*, 159–173. [CrossRef]
- Havenith, H.B.; Strom, A.; Torgoev, I.; Torgoev, A.; Lamair, L.; Ischuk, A.; Abdrakhmatov, K. Tien Shan Geohazards Database: Earthquakes and landslides. *Geomorphology* **2015**, *249*, 16–31. [CrossRef]
- Molnar, P.; Tapponnier, P. Cenozoic Tectonics of Asia: Effects of a Continental Collision: Features of recent continental tectonics in Asia can be interpreted as results of the India-Eurasia collision. *Science* **1975**, *189*, 419–426. [CrossRef] [PubMed]
- Thurman, M. Natural Disaster Risks in Central Asia: A Synthesis. 2011. Available online: https://www.preventionweb.net/files/18945_cadisasterrisksmtd51104.pdf (accessed on 11 April 2011).
- Pavlis, T.L.; Hamburger, M.W.; Pavlis, G.L. Erosional processes as a control on the structural evolution of an actively deforming fold and thrust belt: An example from the Pamir-Tien Shan region, central Asia. *Tectonics* **1997**, *16*, 810–822. [CrossRef]
- Tacconi Stefanelli, C.; Frodella, W.; Caleca, F.; Raimbekova, Z.; Umaraliev, R.; Tofani, V. Assessing landslide damming susceptibility in Central Asia. *Nat. Hazards Earth Syst. Sci.* **2024**, *24*, 1697–1720. [CrossRef]
- Ishihara, K. Liquefaction-induced flow slide in the collapsible loess deposit in Tajik. In *Earthquake Geotechnical Case Histories for Performance-Based Design*; CRC Press: London, UK, 2009; p. 18, ISBN 978-0-429-06211-7.
- Nardini, O.; Confuorto, P.; Intrieri, E.; Montalti, R.; Montanaro, T.; Robles, J.G.; Poggi, F.; Raspini, F. Integration of satellite SAR and optical acquisitions for the characterization of the Lake Sarez landslides in Tajikistan. *Landslides* **2024**, *21*, 1385–1401. [CrossRef]
- Leinss, S.; Bernardini, E.; Jacquemart, M.; Dokukin, M. Glacier detachments and rock-ice avalanches in the Petra Pervogo range, Tajikistan (1973–2019). *Nat. Hazards Earth Syst. Sci.* **2021**, *21*, 1409–1429. [CrossRef]

10. Zafar, A.; Uchimura, T. Case study of slope failure and early warning system of landslides induced by heavy rainfall in Tajikistan, Central Asia. In *Smart Geotechnics for Smart Societies*; CRC Press: London, UK, 2023; p. 4, ISBN 978-1-003-29912-7.
11. Strom, A.; Abdrakhmatov, K. Large-Scale Rockslide Inventories: From the Kokomeren River Basin to the Entire Central Asia Region (WCoE 2014–2017, IPL-106-2). In *Advancing Culture of Living with Landslides*; Sassa, K., Mikoš, M., Yin, Y., Eds.; Springer International Publishing: Cham, Switzerland, 2017; pp. 339–346, ISBN 978-3-319-53500-5.
12. Caleca, F.; Scaini, C.; Frodella, W.; Tofani, V. Regional-scale landslide risk assessment in Central Asia. *Nat. Hazards Earth Syst. Sci.* **2024**, *24*, 13–27. [[CrossRef](#)]
13. Strom, A.L.; Abdrakhmatov, K. *Rockslides and Rock Avalanches of central Asia: Distribution, Morphology, and Internal Structure*; Elsevier: Amsterdam, The Netherlands, 2018; ISBN 978-0-12-803205-3.
14. Haberland, C.; Abdybaev, U.; Schurr, B.; Wetzel, H.; Roessner, S.; Sarnagoev, A.; Orunbaev, S.; Janssen, C. Landslides in southern Kyrgyzstan: Understanding tectonic controls. *Eos Trans. Am. Geophys. Union* **2011**, *92*, 169–170. [[CrossRef](#)]
15. Khasanov, S.; Juliev, M.; Uzbekov, U.; Aslanov, I.; Agzamova, I.; Normatova, N.; Islamov, S.; Goziev, G.; Khodjaeva, S.; Holov, N. Landslides in Central Asia: A review of papers published in 2000–2020 with a particular focus on the importance of GIS and remote sensing techniques. *GeoScience* **2021**, *15*, 134–145. [[CrossRef](#)]
16. Pourghasemi, H.R.; Rahmati, O. Prediction of the landslide susceptibility: Which algorithm, which precision? *Catena* **2018**, *162*, 177–192. [[CrossRef](#)]
17. Ferretti, A.; Savio, G.; Barzaghi, R.; Borghi, A.; Musazzi, S.; Novali, F.; Prati, C.; Rocca, F. Submillimeter Accuracy of InSAR Time Series: Experimental Validation. *IEEE Trans. Geosci. Remote Sens.* **2007**, *45*, 1142–1153. [[CrossRef](#)]
18. Chaussard, E.; Wdowinski, S.; Cabral-Cano, E.; Amelung, F. Land subsidence in central Mexico detected by ALOS InSAR time-series. *Remote Sens. Environ.* **2014**, *140*, 94–106. [[CrossRef](#)]
19. Fiaschi, S.; Wdowinski, S. Local land subsidence in Miami Beach (FL) and Norfolk (VA) and its contribution to flooding hazard in coastal communities along the U.S. Atlantic coast. *Ocean Coast. Manag.* **2020**, *187*, 105078. [[CrossRef](#)]
20. Hilley, G.E.; Bürgmann, R.; Ferretti, A.; Novali, F.; Rocca, F. Dynamics of Slow-Moving Landslides from Permanent Scatterer Analysis. *Science* **2004**, *304*, 1952–1955. [[CrossRef](#)]
21. Fialko, Y.; Sandwell, D.; Simons, M.; Rosen, P. Three-dimensional deformation caused by the Bam, Iran, earthquake and the origin of shallow slip deficit. *Nature* **2005**, *435*, 295–299. [[CrossRef](#)]
22. Bell, R.E.; Studinger, M.; Shuman, C.A.; Fahnestock, M.A.; Joughin, I. Large subglacial lakes in East Antarctica at the onset of fast-flowing ice streams. *Nature* **2007**, *445*, 904–907. [[CrossRef](#)]
23. Ferretti, A.; Fumagalli, A.; Novali, F.; Prati, C.; Rocca, F.; Rucci, A. A New Algorithm for Processing Interferometric Data-Stacks: SqueeSAR. *IEEE Trans. Geosci. Remote Sens.* **2011**, *49*, 3460–3470. [[CrossRef](#)]
24. Berardino, P.; Fornaro, G.; Lanari, R.; Sansosti, E. A new algorithm for surface deformation monitoring based on small baseline differential SAR interferograms. *IEEE Trans. Geosci. Remote Sens.* **2002**, *40*, 2375–2383. [[CrossRef](#)]
25. Faraji Sabokbar, H.; Shadman Roodposhti, M.; Tazik, E. Landslide susceptibility mapping using geographically-weighted principal component analysis. *Geomorphology* **2014**, *226*, 15–24. [[CrossRef](#)]
26. Jolliffe, I.T.; Cadima, J. Principal component analysis: A review and recent developments. *Philos. Trans. R. Soc. Math. Phys. Eng. Sci.* **2016**, *374*, 20150202. [[CrossRef](#)] [[PubMed](#)]
27. Pearson, K. LIII. On lines and planes of closest fit to systems of points in space. *Lond. Edinb. Dublin Philos. Mag. J. Sci.* **1901**, *2*, 559–572. [[CrossRef](#)]
28. Leprince, S.; Barbot, S.; Ayoub, F.; Avouac, J.-P. Automatic and Precise Orthorectification, Coregistration, and Subpixel Correlation of Satellite Images, Application to Ground Deformation Measurements. *IEEE Trans. Geosci. Remote Sens.* **2007**, *45*, 1529–1558. [[CrossRef](#)]
29. Lacroix, P.; Bièvre, G.; Pathier, E.; Kniess, U.; Jongmans, D. Use of Sentinel-2 images for the detection of precursory motions before landslide failures. *Remote Sens. Environ.* **2018**, *215*, 507–516. [[CrossRef](#)]
30. Jawak, S.D.; Kumar, S.; Luis, A.J.; Bartanwala, M.; Tummala, S.; Pandey, A.C. Evaluation of Geospatial Tools for Generating Accurate Glacier Velocity Maps from Optical Remote Sensing Data. In Proceedings of the 2nd International Electronic Conference on Remote Sensing, Online, 22 March–5 April 2017; p. 341.
31. Ayoub, F.; Leprince, S.; Avouac, J.-P. *User's Guide to COSI-CORR: Co-Registration of Optically Sensed Images and Correlation*; California Institute of Technology: Pasadena, CA, USA, 2009.
32. Aschbacher, J.; Milagro-Pérez, M.P. The European Earth monitoring (GMES) programme: Status and perspectives. *Remote Sens. Environ.* **2012**, *120*, 3–8. [[CrossRef](#)]
33. Torres, R.; Snoeij, P.; Geudtner, D.; Bibby, D.; Davidson, M.; Attema, E.; Potin, P.; Rommen, B.; Floury, N.; Brown, M.; et al. GMES Sentinel-1 mission. *Remote Sens. Environ.* **2012**, *120*, 9–24. [[CrossRef](#)]
34. Drusch, M.; Del Bello, U.; Carlier, S.; Colin, O.; Fernandez, V.; Gascon, F.; Hoersch, B.; Isola, C.; Laberinti, P.; Martimort, P.; et al. Sentinel-2: ESA's Optical High-Resolution Mission for GMES Operational Services. *Remote Sens. Environ.* **2012**, *120*, 25–36. [[CrossRef](#)]

35. Leith, W.; Simpson, D.W. Seismic domains within the Gissar-Kokshal Seismic Zone, soviet central Asia. *J. Geophys. Res. Solid Earth* **1986**, *91*, 689–699. [[CrossRef](#)]
36. Immerzeel, W.W.; Bierkens, M.F.P. Asia's water balance. *Nat. Geosci.* **2012**, *5*, 841–842. [[CrossRef](#)]
37. Sidle, R.C.; Caiserman, A.; Jarihani, B.; Khojazoda, Z.; Kiesel, J.; Kulikov, M.; Qadamov, A. Sediment Sources, Erosion Processes, and Interactions with Climate Dynamics in the Vakhsh River Basin, Tajikistan. *Water* **2023**, *16*, 122. [[CrossRef](#)]
38. Evans, S.G.; Hermanns, R.L.; Strom, A.; Scarascia-Mugnozza, G. (Eds.) *Natural and Artificial Rockslide Dams*; Springer Science & Business Media: Berlin, Germany, 2011; Volume 133, ISBN 978-3-642-04763-3.
39. Mamatkanov, D.M.; Murtazayev, U.I.; Tuzova, T.V. Management features of transboundary rivers water resources in central asia in the contemporary context. In *Strengthening the Collaboration Between the Aasa Clean Water Programme and the IAP Water Programme*; Institute for Water and Environmental Problems (SB RAS): Barnaul, Russia, 2009; ISBN 978-5-904061-09-08. Available online: http://84.237.32.8/ru/conf/files/21-22.10.2009/AASA-IAP_1_cover.pdf#page=48 (accessed on 14 April 2025).
40. Abrams, M.; Crippen, R.; Fujisada, H. ASTER Global Digital Elevation Model (GDEM) and ASTER Global Water Body Dataset (ASTWBD). *Remote Sens.* **2020**, *12*, 1156. [[CrossRef](#)]
41. Hartmann, J.; Moosdorf, N. The new global lithological map database GLiM: A representation of rock properties at the Earth surface. *Geochem. Geophys. Geosystems* **2012**, *13*, 2012GC004370. [[CrossRef](#)]
42. Ferretti, A.; Prati, C.; Rocca, F. Permanent scatterers in SAR interferometry. *IEEE Trans. Geosci. Remote Sens.* **2001**, *39*, 8–20. [[CrossRef](#)]
43. Mora, O.; Mallorqui, J.J.; Broquetas, A. Linear and nonlinear terrain deformation maps from a reduced set of interferometric sar images. *IEEE Trans. Geosci. Remote Sens.* **2003**, *41*, 2243–2253. [[CrossRef](#)]
44. Hooper, A.; Zebker, H.; Segall, P.; Kampes, B. A new method for measuring deformation on volcanoes and other natural terrains using InSAR persistent scatterers. *Geophys. Res. Lett.* **2004**, *31*, 2004GL021737. [[CrossRef](#)]
45. Achache, J.; Fruneau, B.; Delacourt, C. Applicability of SAR interferometry for monitoring of landslides. In *ERS Applications, Proceedings of the Second International Workshop, London, UK, 6–8 December 1995*; European Space Agency: Paris, France, 1996; Volume 383, pp. 165–168.
46. Fruneau, B.; Achache, J.; Delacourt, C. Observation and modelling of the Saint-Étienne-de-Tinée landslide using SAR interferometry. *Tectonophysics* **1996**, *265*, 181–190. [[CrossRef](#)]
47. Biggs, J.; Wright, T.J. How satellite InSAR has grown from opportunistic science to routine monitoring over the last decade. *Nat. Commun.* **2020**, *11*, 3863. [[CrossRef](#)]
48. Solari, L.; Del Soldato, M.; Raspini, F.; Barra, A.; Bianchini, S.; Confuorto, P.; Casagli, N.; Crosetto, M. Review of Satellite Interferometry for Landslide Detection in Italy. *Remote Sens.* **2020**, *12*, 1351. [[CrossRef](#)]
49. Wasowski, J.; Bovenga, F. Investigating landslides and unstable slopes with satellite Multi Temporal Interferometry: Current issues and future perspectives. *Eng. Geol.* **2014**, *174*, 103–138. [[CrossRef](#)]
50. Poggi, F.; Montalti, R.; Intrieri, E.; Ferretti, A.; Catani, F.; Raspini, F. Spatial and Temporal Characterization of Landslide Deformation Pattern with Sentinel-1. In *Progress in Landslide Research and Technology*; Alcántara-Ayala, I., Arbanas, Ž., Cuomo, S., Huntley, D., Konagai, K., Mihalić Arbanas, S., Mikoš, M., Sassa, K., Sassa, S., Tang, H., et al., Eds.; Springer Nature: Cham, Switzerland, 2023; Volume 2, pp. 321–329, ISBN 978-3-031-39011-1.
51. Tofani, V.; Segoni, S.; Agostini, A.; Catani, F.; Casagli, N. Technical Note: Use of remote sensing for landslide studies in Europe. *Nat. Hazards Earth Syst. Sci.* **2013**, *13*, 299–309. [[CrossRef](#)]
52. Cigna, F.; Bianchini, S.; Casagli, N. How to assess landslide activity and intensity with Persistent Scatterer Interferometry (PSI): The PSI-based matrix approach. *Landslides* **2013**, *10*, 267–283. [[CrossRef](#)]
53. Berardino, P.; Costantini, M.; Franceschetti, G.; Iodice, A.; Pietranera, L.; Rizzo, V. Use of differential SAR interferometry in monitoring and modelling large slope instability at Maratea (Basilicata, Italy). *Eng. Geol.* **2003**, *68*, 31–51. [[CrossRef](#)]
54. Meng, Q.; Intrieri, E.; Raspini, F.; Peng, Y.; Liu, H.; Casagli, N. Satellite-based interferometric monitoring of deformation characteristics and their relationship with internal hydrothermal structures of an earthflow in Zhimei, Yushu, Qinghai-Tibet Plateau. *Remote Sens. Environ.* **2022**, *273*, 112987. [[CrossRef](#)]
55. Berti, M.; Corsini, A.; Franceschini, S.; Iannaccone, J.P. Automated classification of Persistent Scatterers Interferometry time series. *Nat. Hazards Earth Syst. Sci.* **2013**, *13*, 1945–1958. [[CrossRef](#)]
56. Bekaert, D.P.S.; Handwerger, A.L.; Agram, P.; Kirschbaum, D.B. InSAR-based detection method for mapping and monitoring slow-moving landslides in remote regions with steep and mountainous terrain: An application to Nepal. *Remote Sens. Environ.* **2020**, *249*, 111983. [[CrossRef](#)]
57. Hanssen, R.F. *Radar Interferometry: Data Interpretation and Error Analysis*; Kluwer Academic: Dordrecht, The Netherlands; Boston, MA, USA, 2001; ISBN 978-0-7923-6945-5.
58. Wu, L.; Wang, H.; Li, Y.; Guo, Z.; Li, N. A Novel Method for Layover Detection in Mountainous Areas with SAR Images. *Remote Sens.* **2021**, *13*, 4882. [[CrossRef](#)]

59. Zhang, Y.; Meng, X.; Jordan, C.; Novellino, A.; Dijkstra, T.; Chen, G. Investigating slow-moving landslides in the Zhouqu region of China using InSAR time series. *Landslides* **2018**, *15*, 1299–1315. [[CrossRef](#)]
60. Confuorto, P.; Casagli, N.; Casu, F.; De Luca, C.; Del Soldato, M.; Festa, D.; Lanari, R.; Manzo, M.; Onorato, G.; Raspini, F. Sentinel-1 P-SBAS data for the update of the state of activity of national landslide inventory maps. *Landslides* **2023**, *20*, 1083–1097. [[CrossRef](#)]
61. Festa, D.; Novellino, A.; Hussain, E.; Bateson, L.; Casagli, N.; Confuorto, P.; Del Soldato, M.; Raspini, F. Unsupervised detection of InSAR time series patterns based on PCA and K-means clustering. *Int. J. Appl. Earth Obs. Geoinf.* **2023**, *118*, 103276. [[CrossRef](#)]
62. Chaussard, E.; Farr, T.G. A New Method for Isolating Elastic From Inelastic Deformation in Aquifer Systems: Application to the San Joaquin Valley, CA. *Geophys. Res. Lett.* **2019**, *46*, 10800–10809. [[CrossRef](#)]
63. Yang, W.; Wang, Y.; Wang, Y.; Ma, C.; Ma, Y. Retrospective deformation of the Baige landslide using optical remote sensing images. *Landslides* **2020**, *17*, 659–668. [[CrossRef](#)]
64. Carter, M.; Bentley, S.P. The geometry of slip surfaces beneath landslides: Predictions from surface measurements. *Can. Geotech. J.* **1985**, *22*, 234–238. [[CrossRef](#)]
65. Intrieri, E.; Frodella, W.; Raspini, F.; Bardi, F.; Tofani, V. Using Satellite Interferometry to Infer Landslide Sliding Surface Depth and Geometry. *Remote Sens.* **2020**, *12*, 1462. [[CrossRef](#)]
66. Cruden, D.M. The geometry of slip surfaces beneath landslides: Predictions from surface measurements: Discussion. *Can. Geotech. J.* **1986**, *23*, 94. [[CrossRef](#)]
67. Peppas, M.V.; Mills, J.P.; Moore, P.; Miller, P.E.; Chambers, J.E. Brief communication: Landslide motion from cross correlation of UAV-derived morphological attributes. *Nat. Hazards Earth Syst. Sci.* **2017**, *17*, 2143–2150. [[CrossRef](#)]
68. Dramis, F.; Sorriso-Valvo, M. Deep-seated gravitational slope deformations, related landslides and tectonics. *Eng. Geol.* **1994**, *38*, 231–243. [[CrossRef](#)]
69. Agliardi, F.; Crosta, G.; Zanchi, A. Structural constraints on deep-seated slope deformation kinematics. *Eng. Geol.* **2001**, *59*, 83–102. [[CrossRef](#)]
70. Teshebaeva, K.; Echtler, H.; Bookhagen, B.; Strecker, M. Deep-seated gravitational slope deformation (DSGSD) and slow-moving landslides in the southern Tien Shan Mountains: New insights from InSAR, tectonic and geomorphic analysis. *Earth Surf. Process. Landf.* **2019**, *44*, 2333–2348. [[CrossRef](#)]
71. Ge, Y.; Liu, C.; Tang, H.; Chen, J. Landslide monitoring from point cloud sequence using stereo feature matching. *Earth Surf. Process. Landf.* **2025**, *50*, e70073. [[CrossRef](#)]
72. Ilinca, V.; Şandric, I. A review of UAV-based data applications for landslide mapping and monitoring. In *Earth Observation Applications to Landslide Mapping, Monitoring and Modeling*; Elsevier: Amsterdam, The Netherlands, 2025; pp. 3–36, ISBN 978-0-12-823868-4.

Disclaimer/Publisher’s Note: The statements, opinions and data contained in all publications are solely those of the individual author(s) and contributor(s) and not of MDPI and/or the editor(s). MDPI and/or the editor(s) disclaim responsibility for any injury to people or property resulting from any ideas, methods, instructions or products referred to in the content.